High-Precision Method of Moments Applied to Measurement of Dielectric Parameters at Microwave Frequencies

Jovana G. Petrović, *Graduate Student Member, IEEE*, Dragan I. Olćan, *Member, IEEE*, Nina N. Obradović, and Antonije R. Djordjević

***Abstract*—A novel high-precision model of a custom-made coaxial chamber used for broadband measurement of the relative complex permittivity at microwave frequencies is presented. The model is based on a surface integral-equation formulation of the method of moments tailored for bodies of revolution. All singular integrals encountered in the numerical analysis are calculated in a unified way with a novel integral transformation, which enables precision of up to 12 significant digits using the 64-bit representation of real numbers. The dielectric parameters are estimated from the reflection-coefficient measurement of the chamber with a disk-shaped dielectric sample by comparison of the measured data with the high-precision numerical analysis of the chamber. The complete measurement procedure is illustrated and verified using samples of known dielectric properties.**

***Index Terms*—body of revolution, dielectric measurements, high-precision integration, method of moments, numerical electromagnetics, singular integrals.**

I. INTRODUCTION

ACCURATE measurements of the relative permittivity of various materials (dielectrics) at microwave frequencies are of great importance for applied and theoretical electromagnetics (EM) [1]–[2]. Permittivity measurements have been done both in the time domain and in the frequency domain, and have a long history [3]–[15].

There exist various techniques and different setups of equipment for the measurements of the relative permittivity in the frequency domain, depending on the frequency range, the aggregate state of samples, as well as the shape and the size of samples. Our focus is on solid materials that are linear, homogeneous, and isotropic in the microwave frequency range. Both the relative permittivity, ε_r, and the loss tangent, $\tan\delta$, are contained in the complex permittivity, which is defined by $\varepsilon = \varepsilon_0\varepsilon_r - \mathrm{j}\varepsilon_0\varepsilon_r \tan\delta = \varepsilon_0(\varepsilon_r' - \mathrm{j}\varepsilon_r'')$, where $\varepsilon_0 \approx 8.854$ pF/m is the permittivity of a vacuum, and j is the imaginary unit.

Predominantly, the permittivity measurements have two steps: (1) measurements of a quantity that is related to the permittivity and (2) extraction of the permittivity from the measurement data. The extraction step can include various high-accuracy electromagnetic models of the measurement setups or can be based on certain approximations.

We focus on the permittivity extraction using the full-wave numerical analysis based on the method of moments (MoM) [16]. Recent advancements in MoM and the increase in computer performance have lead to high-precision analysis in acceptable computing time [17]–[21]. The high precision is achieved by calculation of singular and quasi-singular MoM integrals up to the machine precision.

Our measurement setup has rotational symmetry, i.e., it is a body of revolution (BoR) that consists of conductors and dielectrics. BoRs, being a special case of the geometry of EM structures, have been analyzed for over half a century [22]–[25]. However, no high-precision MoM approach has been developed and applied to the high-frequency analysis of BoRs made of composite metallic and dielectric materials. If a surface integral-equation formulation is used for the analysis, the current distribution in a BoR can be a function of one coordinate. Hence, its EM analysis is numerically similar to the analysis of 2-D structures, for which, in [21], a high-precision analysis is presented. However, this analysis cannot be directly applied to BoRs due to different singularities ($\log R$ for 2-D vs. $1/R$ and $1/R^2$ for BoRs). In the technique that we propose, we use polynomials as higher-order basis functions, similarly to [16], [20]–[21]. In [20], only metallic BoRs are analyzed, using a set of basis functions in which some functions belong to multiple (connected) mesh elements. We analyze composite metallic and dielectric BoRs with a different set of basis functions in which basis functions belong exclusively to a single mesh element.

The aim of the present work is twofold. The first goal is to introduce a singularity cancellation transformation that ensures a unified calculation of MoM integrals with high

Manuscript received July 13, 2021, revised September 9, 2021, accepted for publication October 22, 2021. Funds for the realization of this work were partially provided by the Ministry of Education, Science and Technological Development of the Republic of Serbia, Agreement on realization and financing of scientific research work of the School of Electrical Engineering (Record number: 1817/3), and by the Serbian Academy of Sciences and Arts under Grant F133.

J. Petrović, D. Olćan, and A. Djordjević are with the School of Electrical Engineering, University of Belgrade, 11120 Belgrade, Serbia (e-mail: jovanap@etf.bg.ac.rs; olcan@etf.bg.ac.rs, edjordja@etf.bg.ac.rs). A. Djordjević is also with the Serbian Academy of Sciences and Arts (SASA), 11000 Belgrade, Serbia. N. Obradović is with the Institute of Technical Sciences of SASA, 11000 Belgrade, Serbia (e-mail: nina.obradovic@itn.sanu.ac.rs).

precision, up to 12 significant digits (near the theoretical machine precision of 15 significant digits). It is specifically tailored for the MoM analysis of BoRs made of metallic and dielectric domains, with or without losses. We use a MoM surface integral-equation (MoM-SIE) formulation with Galerking testing and Legendre polynomials of arbitrary order as higher-order basis functions.

The second goal is to apply the developed high-precision analysis of BoRs to the extraction step of permittivity measurements in rotationally symmetrical test fixtures (chambers). We use an upgraded version of the coaxial chamber from [26], for which the material samples need to be disk-shaped. Previous quasistatic models of the chamber [27] were used for measurements of ceramic samples [28] at lower frequencies, up to 1000 MHz, while the proposed approach significantly increases the upper frequency limit, deeply into the microwave region.

When the proposed high-precision approach is used, the uncertainty of the numerical results is several orders of magnitude smaller than the uncertainty of the measurements. Hence, the main uncertainty in the extraction of the dielectric parameters is due to the measurements.

The paper is organized as follows. The MoM analysis of BoR numerical models is explained in detail in Section II. In Section III, special attention is devoted to the high-precision numerical integration using a coordinate transformation. In Section IV, the measurement chamber and the hardware setup are briefly presented. The numerical model of the used chamber is described in Section V. Section VI presents results for the complex permittivity, obtained using the proposed model. Finally, concluding remarks are given in Section VII.

II. MoM Analysis of BoR Model

We consider an arbitrary axially symmetrical structure (BoR) that comprises metallic objects and linear piecewise-homogeneous dielectric objects. For the MoM-SIE analysis, based on the equivalence principle and the domain decomposition [16], the input data are the geometry of the BoR, material specifications, and the excitation. The unknowns are the coefficients in the approximations of the surface electric and magnetic currents at the boundary surfaces. The objective is to find the unknown coefficients in the approximations of the surface currents at a given set of frequencies, in the complex domain.

A BoR can comprise several objects that have various electric and magnetic properties. Hence, we consider the BoR as a multiple-region problem [16]. We solve it by using the Poggio-Miller-Chang-Harrington-Wu-Tsai (PMCHWT) formulation [29]. Thereby, the boundary conditions on the surface between regions *i* and *j* are $\mathbf{E}_{\tan}^{(i)} = \mathbf{E}_{\tan}^{(j)}$ and $\mathbf{H}_{\tan}^{(i)} = \mathbf{H}_{\tan}^{(j)}$, where $\mathbf{E}_{\tan}^{(i)}$ and $\mathbf{E}_{\tan}^{(j)}$ are the tangential components of the total (complex) electric fields, and $\mathbf{H}_{\tan}^{(i)}$ and $\mathbf{H}_{\tan}^{(j)}$ are the tangential components of the total (complex) magnetic fields in domains *i* and *j*, respectively. The total fields are due to the excitation and due to the surface electric and magnetic currents and charges, located on the interfaces between adjacent regions.

Our test fixture (i.e., the coaxial chamber) is fed by a coaxial line. Hence, we use a TEM frill to model the excitation [16]. The corresponding rms voltage is $V = 1\,\mathrm{V}$. Upon MoM-SIE analysis, the approximation of currents is known and the network parameters of the chamber can be calculated.

We assume that the surfaces of discontinuities of the analyzed BoR (i.e., surfaces of conductors and dielectric-to-dielectric interfaces) are assembled of BoR elements. Each BoR element is the lateral surface S_f of a conical frustum (depicted in gray in Fig. 1), which is defined by its lower radius a, its upper radius b, and its height L. Each element has its local coordinate system defined by t (the local linear coordinate along a frustum generatirx, $-1 \le t \le 1$, where the radius of the frustum is a at $t = -1$ and b at $t = +1$) and ϕ (the azimuthal angle, $-\pi < \phi \le \pi$). For a point on the frustum whose local coordinates are (t, ϕ), the corresponding Cartesian coordinates are $x = \big((b-a)t + b + a\big)\cos\phi/2$, $y = \big((b-a)t + b + a\big)\sin\phi/2$, and $z = Lt/2$. (Note that special cases of S_f are a cylindrical surface, a flat annular ring, and a circle.)

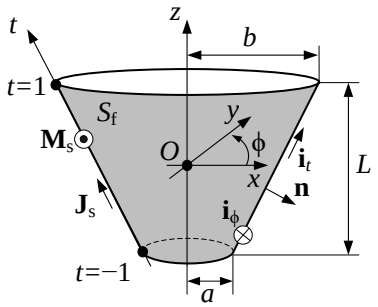

Fig. 1. Axially symmetrical BoR element and its local (t,ϕ) coordinate system.

Due to the axial symmetry of the geometry (BoR) and to the TEM-frill excitation, the currents and charges depend only on the *t*-coordinate. Therefore, if we introduce the unit vectors of the coordinates t and ϕ ($\mathbf{i}_t$ and $\mathbf{i}_\phi$, respectively), the density of surface electric currents $\mathbf{J}_\mathrm{s}$ has only the $\mathbf{i}_t$ component, while the density of the surface magnetic currents $\mathbf{M}_\mathrm{s}$ has only the $\mathbf{i}_\phi$ component.

For each BoR element, we approximate $\mathbf{J}_\mathrm{s}$ and $\mathbf{M}_\mathrm{s}$ by linear combinations of basis functions that depend only on t, as $\mathbf{C}_\mathrm{s} = \sum_{n=0}^{N_0-1} a_n L_n(t)\mathbf{i}_b$, where $\mathbf{C}_\mathrm{s} \in \{\mathbf{J}_\mathrm{s}, \mathbf{M}_\mathrm{s}\}$, $\mathbf{i}_b \in \{\mathbf{i}_t, \mathbf{i}_\phi\}$, $L_n(t)$ is the *n*-th basis function, $a_n \in \{a_n^{(J_\mathrm{s})}, a_n^{(M_\mathrm{s})}\}$ are unknown coefficients ($a_n^{(J_\mathrm{s})}$ for $\mathbf{J}_\mathrm{s}$ and $a_n^{(M_\mathrm{s})}$ for $\mathbf{M}_\mathrm{s}$), and $2N_0$ is the total number of unknown coefficients per element. We use Legendre polynomials of degree n ($n \ge 0$) as the basis

functions $L_n(t)$, since they are orthogonal, which is advantageous for obtaining high accuracy [20]–[21]. Each BoR element has its own set of basis functions, which belong exclusively to that element. Since the continuity of $\mathbf{J}_s$ is not explicitly enforced, in our model there are electric line charges at the edges of the element (i.e., for $t=-1$ and $t=+1$), whose per-unit-length density is, due to the boundary condition, given by $Q'(t=\pm1)=-\frac{\mathrm{j}}{\omega}J_s(t=\pm1)$.

In the electromagnetic model, due to the used domain decomposition, the fields are induced only by the electric and magnetic currents in the same domain. The electric and magnetic fields due to the electric currents and associated charges are given by [16]

$$\mathbf{E}(\mathbf{J}_s)=-\mathrm{j}\omega\frac{\mu}{4\pi}\int_{S'}\frac{\mathbf{J}_s\mathrm{e}^{-\gamma R}}{R}\mathrm{d}S'+ \frac{1}{4\pi\varepsilon}\int_{S'}\frac{(1+\gamma R)\mathrm{e}^{-\gamma R}}{R^2}\rho_s\mathbf{i}_R\mathrm{d}S'+\frac{1}{4\pi\varepsilon}\int_{C'}\frac{(1+\gamma R)\mathrm{e}^{-\gamma R}}{R^2}Q'\mathbf{i}_R\mathrm{d}l', \tag{1}$$

$$\mathbf{H}(\mathbf{J}_s)=\frac{1}{4\pi}\int_{S'}\frac{(1+\gamma R)\mathrm{e}^{-\gamma R}}{R^2}\mathbf{J}_s\times\mathbf{i}_R\mathrm{d}S', \tag{2}$$

where $\mathbf{R}$ is the position-vector of the field point with respect to the source point ($R=|\mathbf{R}|$), $\mathbf{i}_R=\mathbf{R}/R$ is the unit vector of $\mathbf{R}$, ρ_s is the density of the surface electric charges, Q' is the density of the electric line charges, and $\gamma=\mathrm{j}\omega\sqrt{\varepsilon\mu}$ is the (complex) propagation coefficient ($\omega=2\pi f$, where f is the operating frequency). When the material within the considered domain is lossy, ε and μ are complex quantities. The charge density ρ_s is calculated using the continuity equation $\mathrm{div}_s\,\mathbf{J}_s=-\mathrm{j}\omega\rho_s$, where div_s stands for the divergence over the surface where currents exist. Finally, S' is the union of the surfaces over which $\mathbf{J}_s$ and ρ_s are distributed, while C' denotes the union of the edges where Q' is distributed. The electric field due to ρ_s has finite (but different) values at $R=0^+$ and $R=0^-$, while it is not defined at $R=0$, i.e., when the field point is exactly at the surface that carries the charges. In order to avoid $R=0$, we numerically calculate the electric field shifted away from the singularity point for $\xi=10^{-4}\,L$, in the direction perpendicular to S_f.

Due to the axial symmetry and the TEM excitation, $\mathrm{div}_s\mathbf{M}_s=0$. Hence, there are no magnetic surface charges associated with the magnetic currents. In addition, there are no magnetic line charges, because the vector $\mathbf{M}_s$ is tangential to all the edges of the model. Hence, the magnetic and electric fields due to $\mathbf{M}_s$ are given by [16]

$$\mathbf{H}(\mathbf{M}_s)=-\mathrm{j}\omega\frac{\varepsilon}{4\pi}\int_{S'}\frac{\mathbf{M}_s\mathrm{e}^{-\gamma R}}{R}\mathrm{d}S', \tag{3}$$

$$\mathbf{E}(\mathbf{M}_s)=-\frac{1}{4\pi}\int_{S'}\frac{(1+\gamma R)\mathrm{e}^{-\gamma R}}{R^2}\mathbf{M}_s\times\mathbf{i}_R\mathrm{d}S'. \tag{4}$$

All non-vanishing integrals in (1)–(4) can be reduced to the following four integrals over t' and ϕ' (primes denote the source point). By omitting the constants and by designating the local coordinates of the element edges as $t_e'\in\{-1,1\}$ (Fig. 1), the integrals are

$$\mathbf{I}_k(t)=\int_{t'=-1}^{1}\int_{\phi'=-\pi}^{\pi}\mathbf{f}_k(t',\phi')\,\mathrm{d}S'(t',\phi'),\quad k=1,2,3, \tag{5}$$

$$\mathbf{I}_4(t)=\int_{\phi'=-\pi}^{\pi}\mathbf{f}_4(\phi')\,\mathrm{d}l', \tag{6}$$

where $\mathrm{d}S'(t',\phi')=\left((b-a)t'+a+b\right)\sqrt{L^2+(b-a)^2}\,\mathrm{d}\phi'\mathrm{d}t'/4$ and $\mathrm{d}l'=\sqrt{L^2+(b-a)^2}\,\mathrm{d}\phi'/2$, while the integrands are

$$\mathbf{f}_1(t',\phi')=\frac{L_n(t')\mathbf{i}_b\mathrm{e}^{-\gamma R(t',\phi')}}{R(t',\phi')}, \tag{7}$$

$$\mathbf{f}_2(t',\phi')=\frac{(1+\gamma R(t',\phi'))\mathrm{e}^{-\gamma R(t',\phi')}}{R^2(t',\phi')}\mathbf{i}_R\mathrm{div}_s\left(L_n(t')\mathbf{i}_t\right), \tag{8}$$

$$\mathbf{f}_3(t',\phi')=\frac{(1+\gamma R(t',\phi'))\mathrm{e}^{-\gamma R(t',\phi')}}{R^2(t',\phi')}L_n(t')\mathbf{i}_b\times\mathbf{i}_R(t',\phi'),\ \text{and} \tag{9}$$

$$\mathbf{f}_4(\phi')=\frac{(1+\gamma R(t_e',\phi'))\mathrm{e}^{-\gamma R(t_e',\phi')}}{R^2(t_e',\phi')}\mathbf{i}_R L_n(t_e'). \tag{10}$$

By substituting (1)–(4) and the TEM-frill excitation into the boundary conditions and by applying the PMCHWT, we obtain a set of integral equations with unknown coefficients for current approximations. By using the Galerkin testing, these integral equations are transformed into a set of linear equations. Since the integrands are independent of the ϕ-coordinate, the integration over ϕ in the Galerkin testing is omitted. The obtained set of linear equations is given by

$$\int_{t=-1}^{1}L_m(t)\left(\mathbf{F}_{\tan}^{(i)}-\mathbf{F}_{\tan}^{(j)}\right)\frac{(b-a)t+a+b}{4}\sqrt{L^2+(b-a)^2}\,\mathrm{d}t=0, \tag{11}$$

where $m=0,1,\ldots,N-1$, N is the total number of unknowns for all elements in the model, $\mathbf{F}_{\tan}\in\{\mathbf{E}_{\tan},\mathbf{H}_{\tan}\}$, and $\phi=0$. Therefore, there are three numerical integrations to be performed: two for the fields (the first integration over ϕ' and the second one over t') and one for the Galerkin testing procedure (the third integration, which is over t). Note that the integrands (7)–(9) are singular at $R=0$, while the integrand (10) is singular near the edges of the BoR elements. Nonetheless, after the Galerkin integration (11), all the involved integrals have finite values.

By grouping the unknowns on the left-hand side of (11) and the excitation on the right-hand side, we obtain a set of linear equations that can be cast in matrix form as $\mathbf{Ax}=\mathbf{b}$, where $\mathbf{A}_{N\times N}$ is the MoM system matrix, $\mathbf{x}_{N\times1}$ is the column-vector of unknown coefficients, and $\mathbf{b}_{N\times1}$ is the excitation column-vector. Once this system is solved for $\mathbf{x}$, the approximations of the surface currents are obtained. Thereafter, the EM field

at a given point of space can be calculated using (1)–(4).

The precision of **A** has the dominant influence on the precision of the whole analysis. Therefore, the integrations involved in the calculation of the elements of **A** must be performed with high precision, preferably in a unified manner. To that aim, we apply a coordinate transformation prior to the numerical integration. After the transformation, the numerical integration is performed using the standard Gauss-Legendre (GL) procedure. The proposed coordinate transformation is explained in detail in the next section.

III. Coordinate Transformation for High-Precision Integration

The idea of the presented transformation is to stretch-out the region in the vicinity of the singularity so that there are more integration points in regions where the integrand rapidly changes. The transformation is defined as

$$\begin{aligned} t &= |\, s \,|^{m_1-1}\, s(1-\mathrm{sgn}(s)t_\mathrm{m}) + t_\mathrm{m}, \\ \phi &= \pi\, |\, p \,|^{m_2-1}\, p, \end{aligned} \tag{12}$$

where $s \in [-1,1]$ and $p \in [-1,1]$ are new variables, t_m defines the singularity point in the local t-coordinate system, m_1 and m_2 are transformation parameters (positive real numbers), and $\mathrm{sgn}(s)$ is the sign function. Fig. 2 illustrates (12), when $t_\mathrm{m} = 0.5$, for m_1 and m_2 in the range from 2 to 11.

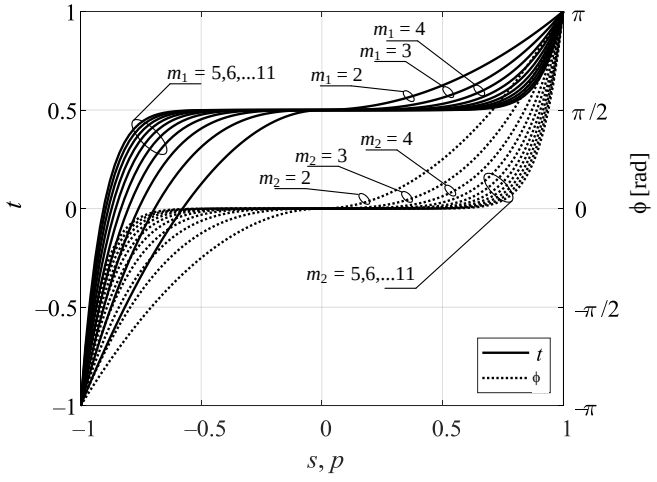

Fig. 2. Illustration of singularity-cancellation transformations.

After applying (12), we obtain $t'(s')$ and $\phi'(p')$ (where primes denote source points). The functions $\mathbf{f}_k(t',\phi')$, $k = 1,2,3$, in the double integrals (5) are transformed into functions $\mathbf{f}_k(t'(s'),\phi'(p'))$, with new variables s' and p', by substituting each t' with $t'(s')$ from (12) and each ϕ' by $\phi'(p')$ from (12), while $\mathbf{f}_4(\phi')$ from the single integral (6) is transformed into $\mathbf{f}_4(\phi'(p'))$, with a new variable p', by substituting each ϕ' by $\phi'(p')$. The elementary surface in (5), $\mathrm{d}S'(t',\phi')$, is converted into $\mathrm{d}S'(t'(s'),\phi'(p'))$ by substituting each t' with $t'(s')$ from (12) and $\mathrm{d}t'\mathrm{d}\phi'$ by $J_{sp}\mathrm{d}s'\mathrm{d}p'$, where J_{sp} is the corresponding Jacobian. So, we obtain a new elementary surface defined by $\mathrm{d}S' = J_{sp}\left((b-a)t'(s')+a+b\right)\sqrt{L^2+(b-a)^2}\,\dfrac{\mathrm{d}p'\mathrm{d}s'}{4}$. Similarly, the elementary length $\mathrm{d}l'(\phi')$ from (6) is converted into $\mathrm{d}l'(\phi'(p')) = J_p\sqrt{L^2+(b-a)^2}\,\mathrm{d}p'/2$, where J_p is the corresponding Jacobian. Finally, the integrals (5)–(6) are transformed into

$$\mathbf{I}_k(t) = \int_{s'=-1}^{1}\int_{p'=-1}^{1} \mathbf{f}_k(t'(s'),\phi'(p'))\mathrm{d}S'(t'(s'),\phi'(p')), \quad k = 1,2,3, \tag{13}$$

$$\mathbf{I}_4(t) = \int_{p'} \mathbf{f}_4(\phi'(p'))\mathrm{d}l'(\phi'(p')), \tag{14}$$

where the corresponding Jacobians are

$$J_s(s',t_\mathrm{m}) = \frac{\mathrm{d}t'}{\mathrm{d}s'} = m_1\,|\,s'\,|^{m_1-1}(1-\mathrm{sgn}(s')t_\mathrm{m}), \tag{15}$$

$$J_p(p') = \frac{\mathrm{d}\phi'}{\mathrm{d}p'} = m_2\pi\,|\,p'\,|^{m_2-1}, \tag{16}$$

$$J_{sp}(s',p',t_\mathrm{m}) = \frac{\mathrm{d}t'}{\mathrm{d}s'}\frac{\mathrm{d}\phi'}{\mathrm{d}p'} = J_s(s',t_\mathrm{m})J_p(p'). \tag{17}$$

Note that the convergence rate of these integrals depends on the order of the basis functions, the position of the singularity point, the operating frequency, and the shape of the BoR element. The convergence is examined in detail in the next subsection.

A. Convergence of Integrals

In order to check the convergence of the integrals, we define a relative error estimate, δ_I, as

$$\delta_I = \frac{|\, I_{N_\mathrm{int}+1} - I_{N_\mathrm{int}} \,|}{|\, I_{N_\mathrm{int}+1} \,|}, \tag{18}$$

where I_{N_int} is the integral value calculated with N_int integration points and $I_{N_\mathrm{int}+1}$ is the value of the same integral calculated with $N_\mathrm{int}+1$ points. If the integral is a surface integral, then N_int is the number of integration points per one integral, i.e., the total number of integration points is N_int^2. If the integral is close to zero, i.e., $\left|I_{N_\mathrm{int}+1}\right| \le 10^{-14}$, the relative error estimate is set to 10^{-14}. This limit is based on the fact that 64-bit double-precision numbers are used, i.e., the machine precision is 15 significant digits.

All of the following numerical experiments are performed on a desktop computer with Windows 10 operating system, Intel(R) Core™ i7-9700 processor, running at 3.00 GHz and using up to 32 GB of memory. The programs are coded in C/C++ programming language and compiled for the maximum execution speed.

The total electric field is calculated based on four integrals, (13) and (14), so we also define an overall (maximum) relative

error estimate as

$$\delta_{\max} = \log_{10}(\max(\delta_{I_k})), \quad (19)$$

where δ_{I_k}, $k = 1, 2, \ldots, 4$, is the relative error estimate (18) of the integral I_k. Note that the number of significant digits of an integral I can be calculated as $\chi = -\log_{10}\delta_I$. Therefore, the negative value of (19), $-\delta_{\max}$, can be interpreted as the approximate number of significant digits.

Our focus is on the singular integrands, when the field point and the source point are at the surface of the same BoR element.

Results in this subsection are given for BoR elements without losses in the materials, and $\varepsilon_r = \mu_r = 1$.

We focus on electrically small BoR elements, due to the application. Hence, (19) is practically independent of frequency.

It is numerically harder to calculate integrals with singularities in the vicinity of the BoR edges than further away from them [21]. Hence, as a representative difficult case, we present results for the integrals with the singularity at $t_m = 0.95$.

1) The Integration Parameters

The maximum relative error estimate (19) as the function of the parameters m_1 and m_2 is presented in Fig. 3 in the case of a cylinder ($a = b = 0.6$ mm and $L = 15.25$ mm), at the operating frequency $f = 3$ GHz. The cylinder is shown in the inset of Fig. 4. The order of the basis functions is $n = 2$ and the number of integration points per integral is $N_{\text{int}} = 300$. This numerical experiment is used to find the optimal values of the parameters m_1 and m_2. From Fig. 3 it can be seen that if $m_1 > 5$ and $5 \le m_2 \le 10$, the number of significant digits is about 12. Further numerical experiments have shown that for other BoR elements results are qualitatively the same.

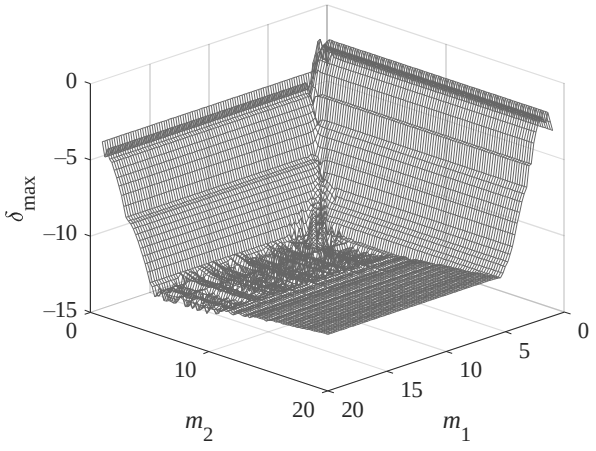

Fig. 3. Maximum relative error estimate for a cylindrical BoR element.

2) Order of Basis Functions

Higher-order basis functions require more integration points than the lower-order ones, for the same accuracy. The maximum error estimate (19) for three BoR elements, when the orders of the basis functions are $n = 4$ and $n = 0$, is presented in Fig. 4. The first considered element is the cylinder used in the previous subsection, the second one is a frustum ($a = 1.0$ mm, $b = 15.0$ mm, and $L = 15.0$ mm), and the third one is an annular ring ($a = 3.0$ mm, $b = 12.2$ mm, and $L = 0$). All BoR elements are shown in the inset of Fig. 4. In addition to these results, results for $\delta_{\max}$ when integrals are calculated without transformation are also shown in Fig. 4. The operating frequency is $f = 3$ GHz. From Fig. 4, it can be concluded that using the proposed transformations, we obtain significantly better precision for the same number of integration points. For example, with around $N_{\text{int}} = 400$, all integrals are calculated with at least 12 significant digits, while for the same number of integration points without the transformation, just one significant digit is obtained. A relatively large number of integration points for small order of basis function is needed, due to the fact that we are interested in the highest precision. However, if lower precision is satisfactory for an application, a smaller number of integration points can be used, according to Fig. 4. Note that if the numerical integration is performed without the singularity cancellation, then positive values of $\delta_{\max}$ are obtained due to the singularity of the integrals. This means that the successively calculated integrals ($I_{N_{\text{int}}}$ and $I_{N_{\text{int}}+1}$) differ for several orders of magnitude. Therefore, MoM integrals must be calculated with the proposed singularity-cancellation approach, or some other numerical technique (e.g. singularity extraction).

To summarize the results from subsections III.A.1-2, if the approximations for the electric and magnetic surface currents are with up to five unknowns each, the integrals (13) and (14) can be calculated with up to 12 significant digits, at an arbitrary field point, with the proposed transformation and the integration setup $m_1 = 7$, $m_2 = 9$, and $N_{\text{int}} = 250$ in the cases of the cylinder and the annular ring, or $N_{\text{int}} = 400$ in the case of the frustum. This setup will be used as the default one in the following subsection.

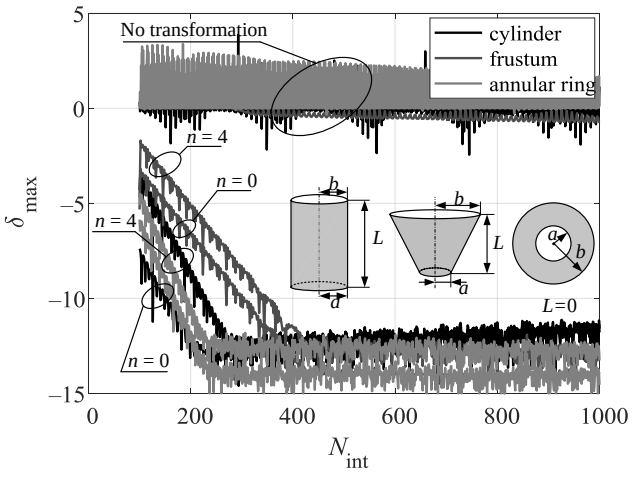

Fig. 4. Maximum relative error estimate for various orders of basis functions.

B. The Galerkin Testing

After the integrals (13) and (14) have been calculated, an additional integration, i.e., the Galerkin testing, is performed to calculate the elements of the MoM system matrix. If the domain of the testing function, $L_m(t)$, and the domain of the source basis function, $L_n(t)$, coincide, the integrand has singular behavior in the vicinity of the edges, i.e., in the vicinity of $t=-1$ and $t=1$. Therefore, before the GL numerical integration, the singularity-cancellation transformation (12) is applied to the integrand two times in a row, as follows.

We use the following notation: $N_{\text{int,g}}$ is the number of integration points for the Galerkin integration, $x_{\text{GL}}(l)$ are the abscissas and $w_{\text{GL}}(l)$ are the weights for the GL integration ($l=1, 2, ..., N_{\text{int, g}}$), t is the coordinate of the field point, and $I(t,n)$ is the integrand. Since the integrands are singular in the vicinity of the edges, (12) is applied to stretch the integrands at the points $t_{\text{m1}}=x_{\text{GL}}(1)$, which is near $t=-1$, and $t_{\text{m2}}=x_{\text{GL}}(N_{\text{int, g}})$, which is near $t=1$. To that purpose, a new integration parameter, m_3, and a new integration coordinate, $s_1=x_{\text{GL}}(l)$, are introduced. The transformation (12) is used to stretch around t_{m1} ($t\equiv s$, $s\equiv s_1$, $t_{\text{m}}\equiv t_{\text{m1}}$, and $m_1\equiv m_3$), and then around t_{m2} ($t\equiv t$, $s\equiv s$, $t_{\text{m}}\equiv t_{\text{m2}}$, and $m_1\equiv m_3$). Now, the matrix element A_{mn}, in the n^{th} column and m^{th} row, is

$$A_{mn}=\sum_{l=1}^{N_{\text{int,g}}} w_{\text{GL}}(l)L_m(t)I(t,n)J_s(s_1,t_{\text{m1}})J_s(s,t_{\text{m2}}), \tag{20}$$

where $J_s(s_1,t_{\text{m1}})$ and $J_s(s,t_{\text{m2}})$ are the Jacobians (15) of the transformation.

The optimal value of m_3 is found using a similar experiment as for m_1 and m_2. In order to illustrate the optimal found value of the parameter $m_3=7$, the relative error estimate (18) is shown in Fig. 5. The error estimate is calculated for the case when there is no transformation and when the integration is done using the transformation. (Note that in all cases the inner integrals are calculated using the proposed transformation, as explained in the previous subsection.) The considered BoR elements are the cylinder, the frustum, and the annular ring, as previously. The operating frequency is $f=3\,\text{GHz}$, and the orders of the basis functions and the testing functions are $n=m=4$.

Even though the number of integration points required to obtain 12 significant digits is $N_{\text{int,g}}=700$, which is about two times more than in the case of integrals (13) and (14), the transformation still yields up to 4 additional significant digits compared to the results without the transformation.

Therefore, the proposed transformation leads to a unified way for calculation of all MoM integrals with high precision. In the following sections, all results are calculated by using $m_1=7$, $m_2=9$, and $m_3=7$ for extraction of the complex permittivity from the measurements. Note that the optimal values of m_1, m_2, and m_3 might be different for each BoR element. However, the used values are chosen so that all integrals are calculated with 12 significant digits.

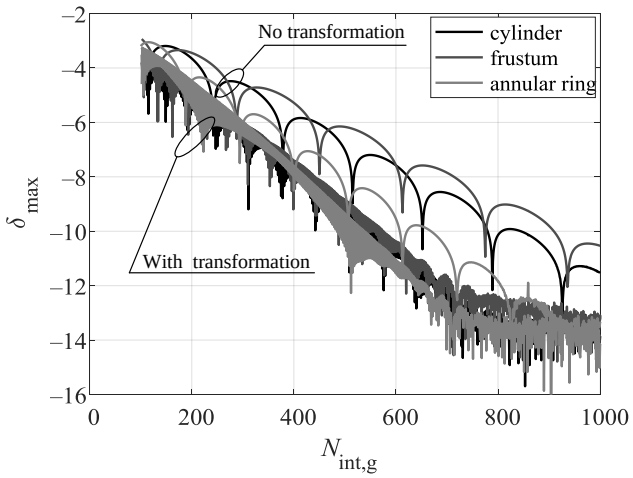

Fig. 5. Relative error estimate of the third (Galerkin) integration.

IV. Measurement Chamber and Hardware Setup

We use a custom-made coaxial chamber [27] for permittivity measurements. The first step is to measure the reflection coefficient of the chamber with the sample placed inside it.

The measurement setup consists of the chamber and a vector network analyzer (NA, Agilent E5061A). The frequency range of the measurements is within 2 MHz to 3 GHz range, which is determined by the NA. A photograph of the setup is shown in Fig. 6, while a photograph of the disassembled chamber and a material sample is shown in the inset of Fig. 6. The material samples are cylindrical, with diameter up to $20\,\text{mm}$ and height up to $14\,\text{mm}$, placed between the plunger and the body of the chamber (see the model cross-section shown in Fig. 7).

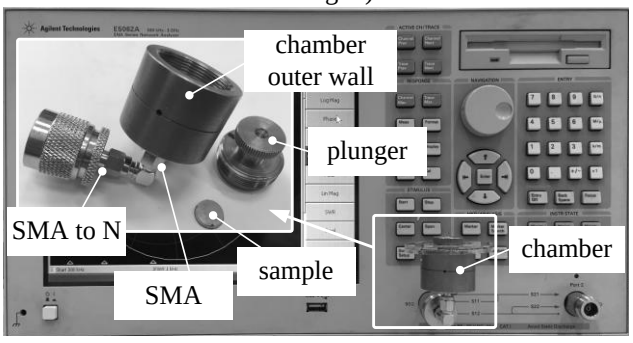

Fig. 6. Photograph of the NA with connected chamber. Disassembled chamber is shown in the inset.

The chamber is made of brass and is fed by the standard SMA (SubMiniature version A) connector with extended PTFE (Teflon), whose outer conductor is connected to the chamber's outer wall, while a metallic annular ring is connected to the inner conductor. The annular ring is supported by a pad made of PTFE. After a material sample is

centered on the annular ring, the chamber is closed by the plunger.

The NA has an N-connector at the port. Hence, a standard SMA-to-N transition is used. Before measurements, a full one-port calibration is performed, so that the reference plane for the measurements of the reflection coefficient is set at the beginning of the SMA connector, as it is marked in Fig. 7.

V. Numerical Model of the Chamber

For the permittivity extraction, as good as possible numerical model of the chamber is needed. Once the numerical model is analyzed, the complex reflection coefficient Γ at the reference plane is calculated for various dielectric parameters of the sample, and compared to the measured reflection coefficient Γ_{meas}. Dielectric parameters that provide the closest values of Γ and Γ_{meas} are declared as the extracted parameters.

Due to the rotational symmetry along the vertical axis, we use the BoR model. The 3-D cross-section of the chamber model is presented in Fig. 7.

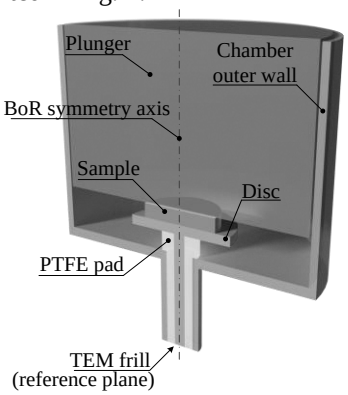

Fig. 7. Cross-section of the numerical model of the chamber (BoR).

There are three different domains (volumes of materials) in the model: the first one is PTFE, which is the dielectric in the used SMA connector and the pad, the second one is air, and the third is the material of the sample, of the unknown (complex) permittivity. The material samples are considered to be non-magnetic; therefore their permeability is set to $\mu_0 = 4\pi \cdot 10^{-7}\,\text{H/m}$. Metal losses are included by the surface impedance for all metallic surfaces as $Z_c = \sqrt{\pi \mu_0 f / \sigma}$, where σ is the electric conductivity. The boundary condition in this case is $\mathbf{E}_{\tan}(\mathbf{J}_s, \mathbf{M}_s) + Z_c \mathbf{J}_s = \mathbf{E}_{\tan}^{\text{exc}}$, where $\mathbf{E}_{\tan}^{\text{exc}}$ is the tangential component of the electric field due to the TEM frill. In the numerical model, this leads to altering the values of the elements on the main diagonal of the MoM system matrix [16], as compared to the lossless case.

The excitation, i.e., the TEM frill, is placed at the reference plane, as it is marked in Fig. 7.

Prior to the permittivity extraction from the measured results, the orders of the current approximations in the model and the number of integration points need to be set. In addition, we want to explore the influence of variations in ε_r on Γ. Therefore, we preformed numerical experiments summarized in the following subsections.

A. Convergence of the Reflection Coefficient

We want to find the parameters of the numerical model that yield results for Γ with a precision higher than can be obtained in the measurements. To that purpose, we calculate Γ for various parameters, at $2\,\text{MHz}$ and $3\,\text{GHz}$, for the chamber with a sample ($\varepsilon_r' = 3.5$ and $\varepsilon_r'' = 10.85 \cdot 10^{-3}$). The total number of BoR elements in the model is 23, the number of unknowns per each BoR element is $N_0 \in \{4, 5, 6\}$, while the number of integration points N_{int}, per integration, is varied from 60 to 160.

The modulus and the argument of Γ are presented in Fig. 8 (the upper panel is for $f = 2\,\text{MHz}$ and the lower panel is for $f = 3\,\text{GHz}$). From Fig. 8 it can be concluded that Γ converges for $N = 5$ and $N_{\text{int}} = 120$ at both frequencies. Therefore, this setup is used for the extraction of the material parameters.

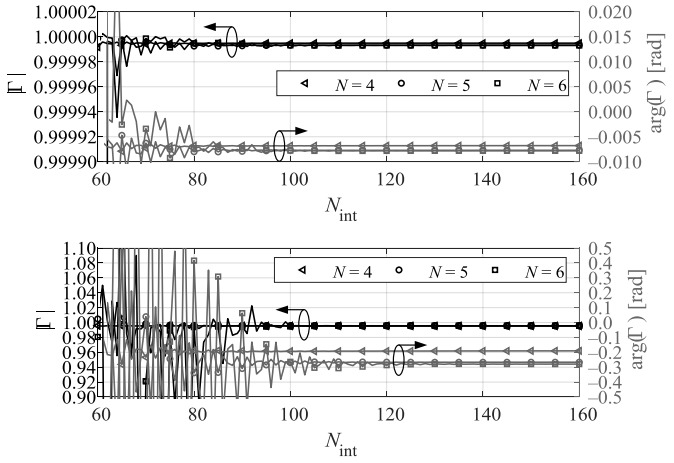

Fig. 8. The modulus and the argument of the reflection coefficient of the chamber: upper panel at f = 2 MHz and lower panel at f = 3 GHz.

B. Comparison with Analytical Solution

In order to check the accuracy of the setup, we analyze a cascaded connection of two sections of coaxial transmission lines, shown in the inset of Fig. 9. The first section is filled by a vacuum, while the second one is filled by a nonmagnetic lossless material of relative permittivity ε_r. The radii of the inner and the outer conductors of the two sections are the same, $a_i = 0{,}6\,\text{mm}$ and $b_i = 2{,}025\,\text{mm}$. The length of each section is $L = 6\,\text{mm}$. (The dimensions of coaxial transmission lines are chosen so that they are of the same order of magnitude as the dimensions of the coaxial feed of the chamber.) The port with the nominal impedance of $50\,\Omega$ is placed at the beginning of the first line, while the end of the second line is short-circuited. The reflection coefficient is calculated both analytically (Γ_{theory}) and using the proposed numerical approach (Γ). In the numerical model, the TEM-

frill excitation is placed at the beginning of the first section. The relative permittivity is varied in the range $1 \le \varepsilon_r \le 100$. The results for the relative errors of Γ, namely $\dfrac{\left|\Gamma_{\text{theory}} - \Gamma\right|}{\left|\Gamma_{\text{theory}}\right|}$, are presented in Fig. 9 for frequencies 30 MHz, 300 MHz, and 3 GHz.

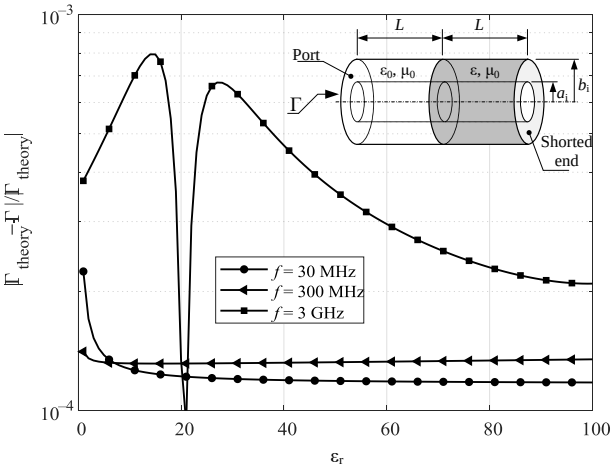

Fig. 9. Relative error of Γ as a function of ε_r at 30 MHz, 300 MHz, and 3 GHz.

The results presented in Fig. 9 show that the relative error of Γ is below 0.1 % for all considered frequencies and all considered relative permittivities. This relative error is below the errors of the measurement setup. Hence, the model is sufficiently accurate for the present application.

Note that the increase of the relative error of Γ in Fig. 9 for higher frequencies is due to the fact that the same numerical setup (i.e., the same number of basis functions and integration points) is used for all presented frequencies. Higher accuracy can be achieved if the number of basis functions is increased.

With the aim to determine the influence of the number of significant digits, *p*, of the elements of the MoM system matrix to the accuracy of Γ, an additional numerical experiment is performed. We start from the system matrix with all elements calculated with at least 12 significant digits. In each sequential step, one digit is changed to zero starting from the least significant digit. This is repeated until we get only one significant digit. The same procedure is simultaneously applied to the excitation vector, i.e., the free column vector. For each *p*, the resulting linear system is solved, the reflection coefficient is calculated, and the relative error is compared to the theoretical solution. The operating frequency is f = 300 MHz and $1 \le \varepsilon_r \le 100$. Fig. 10 shows the relative errors of the reflection coefficients calculated with $p = 1, 2, \ldots, 14$ significant digits for higher-order basis functions. Since the system matrix is calculated with 12 accurate significant digits, the relative errors for $p \in \{14, 13, 12\}$ are practically the same. When $p = 11$, we can see small discrepancies. Reducing the number of significant digits leads to the reduction in the accuracy of the reflection coefficient. Obviously, it is sufficient to calculate the system matrix with $p = 9$ significant digits to keep the relative error below 0.1 %.

Finally, we make a comparison between a low-order approximation (polynomial of degree one) and a higher-order approximation (polynomial of degree eight). As low-order approximations we consider polynomials of the order of zero or one, while higher-order approximations are all polynomials of degree higher than one. The low-order model has the largest segment of length l = 1 mm. As the operating frequency is f = 300 MHz, the electrical length of the largest segment is $l/\lambda = 0.01$ in the dielectric with $\varepsilon_r = 100$. The results are obtained with integrals calculated with either 2 or 3 significant digits. The total analysis time for the low-order approximation with $p = 3$ is practically the same as the time needed for the higher-order approximation with $p = 12$. The result presented in Fig. 10 shows that for the same amount of time, the higher-order approximation leads to one order of magnitude lower relative error. Therefore, for the high precision analysis, a higher-order approximation is needed.

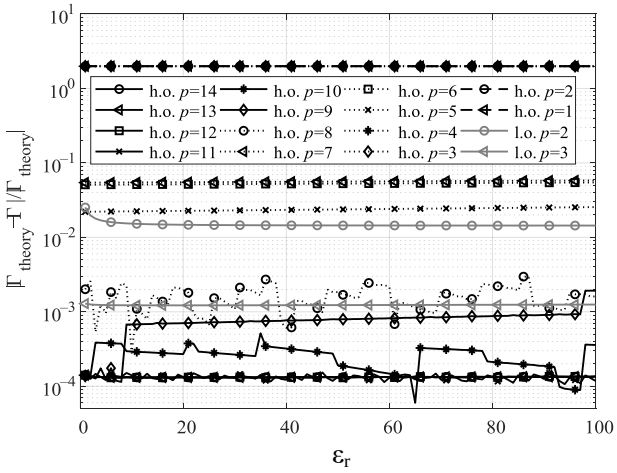

Fig. 10. Relative errors of Γ for matrix elements calculated with different number of significant digits, *p*, with either higher-order (h.o.) or low-order (l.o.) basis functions.

C. Influence of Variations of Permittivity on Reflection Coefficient

We consider the coaxial chamber shown in Fig. 7 and assume that we know the dimensions of the measured sample. In order to prepare tools for the estimation of the relative permittivity of the sample (ε_r) from the measured data, we use the numerical model to investigate the relation between ε_r and the reflection coefficient at the reference plane (Γ), i.e., we consider the function $\Gamma(\varepsilon_r)$. The analytic form of this function is not known. However, if we consider small variations of ε_r, the corresponding variations of Γ are expected to be practically linearly proportional to the variations of ε_r (Taylor expansion).

To prove this assumption, we calculate the absolute change

in Γ normalized to the relative change of ε_r, namely $|\Delta\Gamma| \Big/ \left|\frac{\Delta\varepsilon_r}{\varepsilon_r}\right|$. For a given frequency and small variations of ε_r this ratio should be constant (but different for different frequencies and different complex permittivities). The results are presented in Fig. 11 for $\varepsilon_r' = 3.5$, $\varepsilon_r'' = 10.85 \cdot 10^{-3}$, $d = 10.4\,\text{mm}$ and $h = 1.6\,\text{mm}$. Indeed, in the range $10^{-10} \le |\Delta\varepsilon_r/\varepsilon_r| \le 10^{-2}$, the ratio is constant, which illustrates the overall numerical stability of the model. When $|\Delta\varepsilon_r/\varepsilon_r| < 10^{-10}$, we enter into numerical noise of the differencing. Hence, the results become erratic. On the other hand, when the variations of ε_r become large (e.g., $|\Delta\varepsilon_r/\varepsilon_r| > 10^{-2}$), the linearity does not hold any more because higher-order terms in the Taylor expansion become important.

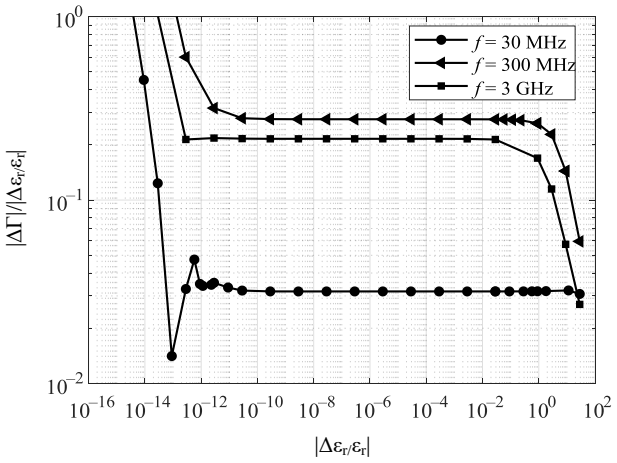

Fig. 11. The absolute change of Γ normalized to relative variations of ε_r.

The results from Fig. 11 can be used to estimate the relative error of extracted ε_r in the following way. If the measurement uncertainty of Γ is $|\Delta\Gamma/\Gamma| \approx 1.5\,\%$, then $|\Delta\varepsilon_r/\varepsilon_r| \approx \frac{1}{K}|\Delta\Gamma|$ (assuming $|\Gamma| \approx 1$), where, from Fig. 11, $K \approx 0.3$ is a constant (for $10^{-10} \le |\Delta\varepsilon_r/\varepsilon_r| \le 10^{-2}$) at 300 MHz. Hence, $|\Delta\varepsilon_r/\varepsilon_r| \approx 5\,\%$ is the relative error of the extracted ε_r at 300 MHz.

VI. Measuring Relative Permittivity of Material Samples

Using the proposed high-precision BoR model and the outlined measurement setup, the relative permittivity of Teflon is measured. This material is chosen as a benchmark example since its relative permittivity is well known.

At frequencies up to 3 GHz, the real part of the relative permittivity of Teflon is around $\varepsilon_r' = 2$ and the imaginary part is very small, $\varepsilon_r'' \le 10^{-4}$. Hence, only ε_r' is determined here. Measurement of Teflon is challenging because we used samples whose diameter is more than two times smaller than the diameter of the chamber and the relative permittivity is small (i.e., it is a low-contrast material). Hence, the influence of the measured sample on Γ is relatively small.

The extraction of ε_r' is done by minimizing the discrepancy between measured and calculated Γ at each considered frequency. Moreover, ε_r' obtained at the previous frequency is used as the starting point for the minimization at the next frequency (i.e., we use tracking). The tracking solves the problem of possible multiple solutions of ε_r', by using the fact that ε_r' does not change significantly between successive frequencies (since Teflon is a low-loss material).

Four samples of diameter 10 mm and thickness 2 mm, 3 mm, 4 mm, and 5 mm are considered. The real part of the relative permittivity is extracted at eight frequencies in the range from 300 MHz to 2.4 GHz and results are presented in Fig. 12. From this figure, it can be seen that the relative error of the extracted ε_r' is around $\pm 5\,\%$. Namely, the maximal measurement uncertainty of $|\Delta\Gamma/\Gamma|$ is estimated to be 0.5 %. Using the estimation of K from Fig. 11, this leads to the measurement uncertainty of ε_r' around $\pm 5\,\%$. Note that the measurement uncertainty is due to various factors, e.g., the measurement error of the physical dimensions of the chamber and the sample, the surface flatness of the sample and the chamber (which is important for high-permittivity samples), the pressure of the plunger (which is important for soft samples, like Teflon), the actual position of the sample (i.e., the offset from the central position, which is important for very high frequencies), the measurement uncertainty of the NA, etc.

The measurement results verify the proposed numerical model and the measurement procedure.

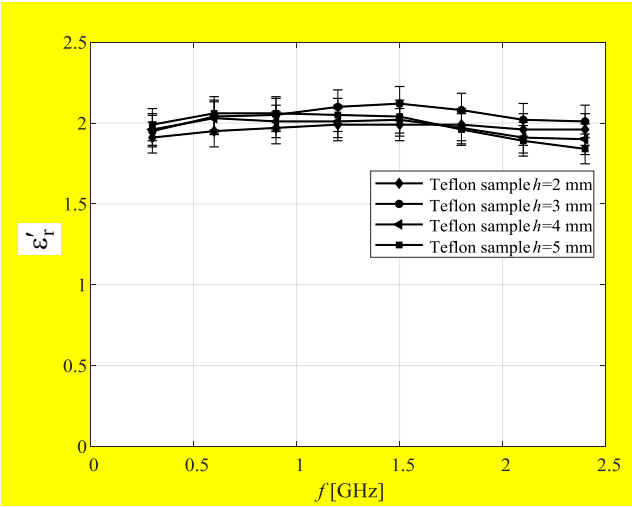

Fig. 12. Relative permittivity extracted from the measurements of the reflection coefficient for Teflon samples.

VII. Conclusions

The singularity-cancellation transformation for the numerical integration in the analysis of BoRs, using MoM-SIE based on domain decomposition, is presented in this work.

Using this transformation, all the encountered MoM integrals can be calculated up to 12 significant digits in a unified way, using 64-bit representation of real numbers.

The high-precision numerical model based on the proposed approach is applied to the extraction of the relative complex permittivity at microwave frequencies, because it yields results of higher accuracy than can be achieved in the measurements setup.

The obtained results for the measurements of samples of known permittivities verify the procedure for extraction of dielectric parameters as well as the proposed high-precision numerical model. Finally, the proposed numerical model can be used for higher frequencies, where resonance of the chamber occurs, which is the work in progress.

REFERENCES

[1] D. M. Pozar, *Microwave Engineering*, John Willy and Sons, USA, 2012, ch. 2, pp. 48-94.

[2] H. Johnson and M. Graham, *High-Speed Digital Design*, Prentice Hall PTR, New Jersey. 1993, ch. 5, pp. 189-221.

[3] A. M. Nicolson, G. F. Ross, "Measurement of the intrinsic properties of materials by time domain techniques," *IEEE Trans. Instrum. Meas.*, vol. IM–19, no. 4, pp. 377-382, 1970.

[4] M. C. Decerton, F. E. Gardiol, "Simple nondestructive method for measurement of complex permittivity," *IEEE Trans. Instrum. Meas.*, vol. 23, no. 4, pp. 434-438, 1974.

[5] M. C. Decreton, M. S. Ramachandriah, "Nondestructive measurement of complex permittivity for dielectric slabs," *IEEE Trans. Microw. Theory and Techniques*, vol. 23, no. 12, pp. 1077-1080, 1975.

[6] D. K. Ghodgaonkar, V. V. Varadan, "A free-space method for measurement of dielectric constants and loss tangents at microwave frequencies," *IEEE Trans. Instrum. Meas.*, vol. 37, no. 3, pp. 789-793, 1989.

[7] D. Misra, M. Chabbra, B. R. Epstein, M. Mirotznik, K. Foster, "Noninvasive electrical characterization of materials at microwave frequencies using an open-ended coaxial line: test of an improved calibration technique," *IEEE Trans. Microw. Theory and Techniques*, vol 38, no. 1, pp. 8-14, 1990.

[8] D. Misra, "On the measurement of the complex permittivity of materials by an open-ended coaxial probe," *IEEE Microw. and Guided Letters*, vol. 5, no. 5, pp. 161-163, 1995.

[9] K. J. Bois, A. Benally, R. Zoughi, "Multimode solution for the reflection properties of an open-ended rectangular waveguide radiating into a dielectric half-space: The forward and inverse problems," *IEEE Trans. Instrum. Meas.*, vol. 48, no. 6, pp. 1131-1140, 1999.

[10] A. R. Djordjević, R. M. Biljić, V. D. Likar-Smiljanić, T. K. Sarkar, "Wideband frequency-domain characterization of FR-4 and time-domain causality," *IEEE Trans. Electromagnetic Compatibility*, vol. 43, pp. 662-667, 2001.

[11] I. Huynen, C. Steukers, F. Duhamel, "A wideband line-line dielectrometric method for liquids, soils, and planar substrates," *IEEE Trans. Instrum. Meas.*, vol. 50, no. 5, pp. 1343–1348, 2001.

[12] M. W. Hyde, M. J. Havrilla, A. E. Bogle, N. J. Lehman, "Broadband Characterization of Materials Using a Dual-Ridged Waveguide," *IEEE Trans. Instrum. Meas.*, vol. 62, no. 12, pp. 3168-3176, 2013.

[13] M. W. Hyde, M. J. Havrilla, A. E. Bogle, "Nondestructive Determination of the Permittivity Tensor of a Uniaxial Material Using a Two-Port Clamped Coaxial Probe," *IEEE Trans. Microw. Theory and Techniques*, vol. 64, no. 1, pp. 239-246, 2016.

[14] J. Dong et al. "Noncontact Measurement of Complex Permittivity of Electrically Small Samples at Microwave Frequencies," *IEEE Trans. Microw. Theory and Techniques*, vol 64, no. 9, pp. 2883-2893, 2016.

[15] U. C. Hasar, Y. Kaya, "Self-Calibrating Noniterative Complex Permittivity Extraction of Thin Dielectric Samples," *IEEE Trans. Electromagnetic Compatibility*, vol. 60, no. 2, pp. 354-361, 2018.

[16] B. M. Kolundžija, A. R. Djordjević, *Electromagnetic Modeling of Composite Metalic and Dielectric Structures*, Artech House, Boston, London, 2002, ch. 3, pp. 116-119, ch. 4, pp. 171-176, pp. 179-182, pp. 333-337.

[17] M. Khayat, D. Wilton, "Numerical evaluation of singular and near-singular potential integrals," *IEEE Trans. Antennas and Propag.*, vol. 53, no. 10, pp. 3180-3190, 2005.

[18] R. Graglia and G. Lombardi, "Machine precision evaluation of singular and nearly singular potential integrals by use of Gauss quadrature formulas for rational functions," *IEEE Trans. Antennas and Propag.*, vol. 56, no. 4, pp. 981-998, 2008.

[19] A. Polimeridis, F. Vipiana, J. Mosig, D. Wilton, "DIRECTFN: Fully numerical algorithms for high precision computation of singular integrals in Galerkin SIE methods," *IEEE Trans. Antennas and Propag.*, vol. 61, no. 6, pp. 3112-3122, 2013.

[20] A. J. Krneta, B. M. Kolundžija, "Evaluation of potential and impedance integrals in analysis of axially symmetric metallic structures to prescribed accuracy up to machine precision," *IEEE Trans. Antennas and Propag.*, vol. 65, no. 5, pp. 2526-2539, 2017.

[21] J. G. Perović, D. I. Olćan, B. M. Kolundžija, A. R. Djordjević, "A singularity cancellation transformation for entire domain analysis of 2-D structures with high precision integration," *IEEE Transactions on Antennas and Propagation*, vol. 67, no. 4, pp. 2522-2533, 2019.

[22] M. G. Andreasen, "Scattering from bodies of revolution," *IEEE Trans. Antennas Propag.*, vol. 13, pp. 303–310, 1965.

[23] A. W. Glisson and D. R. Wilton, "Simple and efficient numerical methods for problems of electromagnetic radiation and scattering from surfaces," *IEEE Trans. Antennas Propag.*, vol. 28, no. 5, pp. 593–603, 1980.

[24] S. D. Gedney and R. Mittra, "The use of the FFT for the efficient solution of the problem of electromagnetic scattering by a body of revolution," *IEEE Trans. Antennas Propag.*, vol. 38, no. 3, pp. 313–322, 1990.

[25] Jean-Pierre A. H. M. Vaessen, Martijn C. van Beurden, and Anton G. Tijhuis, "Accurate and Efficient Computation of the Modal Green's Function Arising in the Electric-Field Integral Equation for a Body of Revolution," *IEEE Trans. on Antennas Propag.*, vol. 60, no. 7, pp. 3294-3304, 2012.

[26] A. Đorđević, J. Dinkić, M. Stevanović, D. Olćan, S. Filipović, N. Obradović, "Measurement of permittivity of solid and liquid dielectrics in coaxial chambers," *Microwave Review*, vol. 22, no. 2, pp. 3-9, 2016.

[27] A. Djordjević, D. Olćan, J. Petrović, N. Obradović, S. Filipović, "High-accuracy quasistatic model for bodies of revolution tailored for RF measurements of dielectric parameters", *Facta Universitatis Series: Electronics and Energetics*, vol. 34, no. 1, pp. 141-156, 2021.

[28] N. Obradović, W. G. Fahrenholtz, S. Filipović, D. Kosanović, A. Dapčević, A. Đorđević, I. Balać, V. B. Pavlović, "The effect of mechanical activation on synthesis and properties of MgAl2O4 ceramics", *Ceramics Int.*, vol. 45, no. 9, pp. 12015-12021, 2019.

[29] A.J. Poggio, E.K. Miller, "Integral Equation Solutions of Three-dimensional Scattering Problems," in *Computer Techniques for Electromagnetics*, R. Mittra (ed.), Oxford UK, Pergamon, 1973, ch. 4, pp. 159-264.

Jovana G. Petrović (M'18) was born in Kraljevo, Serbia, in 1992. She received the B.Sc. and M.Sc. degrees in electrical engineering from the School of Electrical Engineering, University of Belgrade in 2015 and 2016, respectively. She is currently pursuing the Ph.D. degree in the

same school. Her current research interests are numerical and applied electromagnetics and optimization algorithms.

Dragan I. Olćan (S'05-M'09) is an Associate Professor at the School of Electrical Engineering, University of Belgrade, Serbia. At the same school he received his B.Sc. (5 years), M.Sc., and Ph.D. degrees in 2001, 2004, and 2008, respectively. He is a coauthor of three commercial electromagnetic software codes, twenty journal papers, eighty conference papers, and seven textbooks. His main research interests are: numerical electromagnetic analysis, optimization algorithms applied to electromagnetic design, and electromagnetic compatibility.

Nina N. Obradović was born in Belgrade, Serbia, on March 25, 1977. She received the B.Sc., M.Sc., and Ph.D. degrees in physical chemistry from the University of Belgrade, Belgrade, Serbia, in 2001, 2005, and 2007, respectively.

In 2002, she joined the Institute of technical sciences of the Serbian Academy of Sciences and Arts, as a junior research assistant. She was promoted to a research associate, senior research associate, and principal research fellow, in 2005, 2008, and 2012, respectively. Dr. Obradovic is a Member of the Scientific council of Science Fund of the Republic of Serbia from 2019-2023. She has authored or coauthored about 80 papers in international journals, 1 monograph, 1 technical solution and has over 80 conference presentations. Teaches "Thermal Analysis-Methods and Applications" and "Processing of Ceramic Materials" under the doctoral study Electrical and Computer Engineering, Department of modern materials and technologies of the electronics, the Technical Faculty, Cacak, Kragujevac University. Areas of her scientific interest are ceramics, powder processing, nanopowders, kinetics and sintering.

Dr. Obradovic is an Editor in Science of Sintering journal and a Reviewer for the Journal of Thermal Analysis and Calorimetry, Journal of Alloys and Compounds, Ceramics International, Powder Technology, Journal of American Ceramic Society, Electrochemical and Solid State Letters, Processing and Application of Ceramics, International Journal of Molecular Sciences, Journal of Material Science, Termochimica Acta, Journal of Advanced Ceramics, International Journal of Mechanical Sciences.

Antonije R. Djordjević was born in Belgrade, Serbia, on April 28, 1952. He received the B.Sc., M.Sc., and Ph.D. degrees in electrical engineering from the University of Belgrade, Belgrade, Serbia, in 1975, 1977, and 1979, respectively.

In 1975, he joined the School of Electrical Engineering, University of Belgrade, as a Teaching Assistant. He was promoted to an Assistant Professor, an Associate Professor, and a Professor, in 1982, 1988, and 1993, respectively. In 1983, he was a Visiting Associate Professor at Rochester Institute of Technology, Rochester, NY, USA. He was also an Adjunct Scholar with Syracuse University, Syracuse, NY, USA. In 1997, he became a Corresponding Member of the Serbian Academy of Sciences and Arts, and a Full Member in 2006. He has authored or coauthored about 300 papers (90 of which were published in leading international journals), and coauthored 3 monographs, 2 chapters in monographs, 9 monographs with software (all monographs published in the USA), and 16 textbooks at the university level (in Serbian). His research interests include numerical electromagnetics, in particular applied to fast digital signal interconnects, wire and surface antennas, microwave passive circuits, and electromagnetic-compatibility problems.

Dr. Djordjevic has been a Reviewer for the IEEE Transactions on Microwave Theory and Techniques, the IEEE Transactions on Antennas and Propagation, and other journals.